

# Quantitative phase and refractive index measurements with point-source digital in-line holographic microscopy

M. H. Jericho,<sup>1,\*</sup> H. J. Kreuzer,<sup>1</sup> M. Kanka,<sup>2</sup> and R. Riesenber<sup>2</sup>

<sup>1</sup>Department of Physics and Atmospheric Science, Dalhousie University, Halifax, Nova Scotia B3H3J5, Canada

<sup>2</sup>Institute of Photonic Technology, Albert-Einstein-Strasse 9, 07747 Jena, Germany

\*Corresponding author: Jericho@fizz.phys.dal.ca

Received 23 September 2011; revised 14 November 2011; accepted 15 November 2011; posted 15 November 2011 (Doc. ID 154883); published 28 March 2012

Point-source digital in-line holographic microscopy with numerical reconstruction is ideally suited for quantitative phase measurements to determine optical path lengths and to extract changes in refractive index within accuracy close to 0.001 on the submicrometer length scale. This is demonstrated with simulated holograms and with detailed measurements on a number of different micrometer-sized samples such as suspended drops, optical fibers, as well as organisms of biological interest such as *E. coli* bacteria, HeLa cells, and fibroblast cells. © 2012 Optical Society of America

OCIS codes: 110.0110, 110.2960, 110.5086, 090.0090, 090.1995.

## 1. Introduction

Point-source digital in-line holographic microscopy (PSDIHM) is capable of generating intensity and amplitude images of objects with submicrometer resolution [1–6]. The hologram reconstruction transforms, however, also give access to phase information and images of the spatial variations of phase shifts of the wave fronts in the optic field are easily created. The quantitative determination of phase shifts is an integral part of digital in-line holographic microscopy (DIHM) so that unlike the situation in standard optical phase microscopy, a quantitative determination of the optical path through an object is easily accomplished. Classical interferometric phase shift measurements are capable of very high sensitivity but are often cumbersome to employ. The simplicity of DIHM, and, in particular, of PSDIHM, makes it of great interest to determine to what extent accurate optic path measurements on micrometer-sized objects are possible with PSDIHM. A theoretical and experi-

mental analysis of PSDIHM hologram recording and reconstruction was recently published by Qu *et al.* [7]. The authors suggested that because of twin-image problems that can arise in PSDIHM, phase reconstructions do not represent the quantitative phase delay induced by the specimen. Our objective in this work is to show that this criticism is unwarranted and that quantitative phase measurements are possible with PSDIHM. We will also explore the advantages of PSDIHM phase image analysis and discuss its limitations.

To determine the reliability of PSDIHM measured optic paths, we made measurements on objects whose relevant parameters were already known or were determined by other measuring techniques. Our measurements therefore include suspended drops, optical fibers, as well as organisms of biological interest such as *E. coli* bacteria, HeLa cells, and fibroblast cells. To minimize the effects of inevitable uncertainties in sample size and refractive index values that one encounters in real samples, we also created simulated PSDIHM holograms of objects with specified geometry, dimensions, and refractive indexes. These holograms were then reconstructed

with PSDIHM software and the resulting object dimension and refractive indexes were compared with the actual values that were used to create the holograms leading to excellent agreement in most cases.

In Gabor [8] geometry PSDIHM, a laser illuminated pinhole emits spherical waves that travel towards a CCD photo sensor chip positioned along the optic path. When objects are placed between the pinhole and the detector, waves scattered by the objects, combine with unscattered waves (the reference wave) at the detector to form an interference pattern or hologram. This hologram consists of a complex pattern of fringes that contain all the position information about the imaged objects. To recover the object image, the hologram undergoes a pixel by pixel numerical reconstruction. In our work, this reconstruction is achieved in selected image planes with the Helmholtz–Kirchhoff transform [1,6]:

$$K(\vec{r}) = \int_S d^3\xi \tilde{I}(\vec{\xi}) \exp[2\pi i \vec{\xi} \cdot \vec{r} / \lambda \xi]. \quad (1)$$

Here the integration extends over the two-dimensional surface of the screen (assumed to be perpendicular to the optical axis) with coordinates  $\xi = (X, Y, L)$ , where  $L$  is the distance from the source (pinhole) to the center of the screen (CCD chip) and  $\tilde{I}(\xi)$  is the contrast image (hologram) on the screen, obtained by subtracting the images with and without the object present. The function  $K(r)$  is significantly structured and differs from zero only in the space region occupied by the object. By reconstructing the wavefront  $K(r)$  on a number of planes at various distances from the source in the vicinity of the object, a three-dimensional (3D) image can be built up from a single two-dimensional hologram. A reconstruction plane that contains a sharp image of an object is

equivalent to an in-focus plane in conventional optical microscopy.  $K(r)$  is a complex function and one usually plots the intensity  $KK^*$  to represent the object, although phase images are also available from  $K$ . The phase image of objects is obtained from  $K(r)$  by evaluating the phase angle:

$$\psi(r) = \arctan \frac{\text{Im} K(r)}{\text{Re} K(r)}.$$

Holography depends on phase shifts and interference of light waves. If the space between the point source and the screen is filled with a medium of refractive index  $n > 1$ , the interference pattern on the screen will be formed with light of shorter wavelength and the hologram will generally show more fringes and will give better resolution. When light travels through several media between the point source and screen, each medium with its own refractive index, then the interference pattern on the screen (i.e. the hologram) is determined by an effective wavelength that depends on how far light travels in each medium [9].

The spherical wave fronts from the pinhole lead to phase wrapped patterns when holograms are phase reconstructed in selected planes. This is illustrated in Fig. 1A. The point source at  $P$  emits spherical waves which have radius  $R$  when they meet the reconstruction plane. Rays that are propagating at an angle  $\theta$  have an extra phase shift, given by the extra distance  $S$ , before they meet the reconstruction plane. As function of the distance from the center,  $w$ , this extra phase shift is

$$\Phi = (2\pi/\lambda)S = (2\pi/\lambda)[(R^2 + w^2)^{1/2} - R]. \quad (2)$$

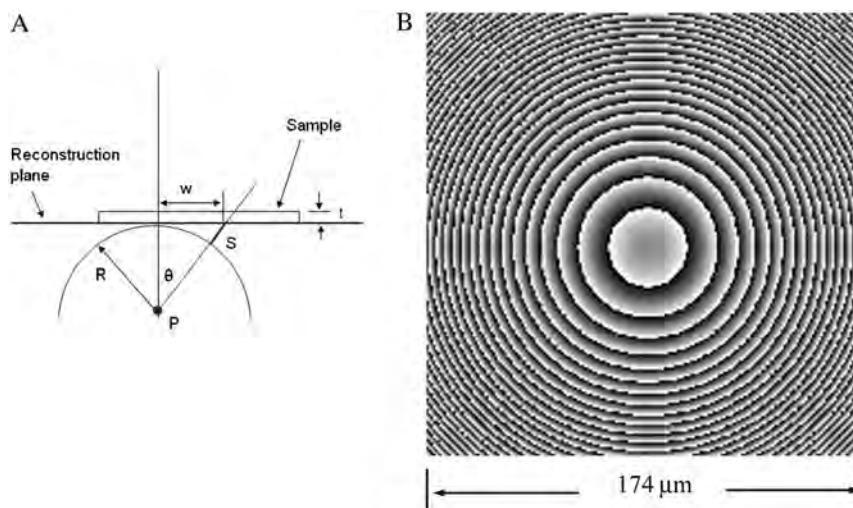


Fig. 1. A. Schematic drawing of a spherical wave front of radius,  $R$ , contacting a reconstruction plane when a phase image of a sample is generated. The phase shift at a distance,  $w$ , from the optic axis is determined by the extra distance,  $S$ , the wave front has to travel to reach the reconstruction plane. The phase range is limited to  $2\pi$  so that the phase is reset back to zero every multiple of  $2\pi$ . This leads to the characteristic concentric ring structure of a phase reconstruction in point-source DIHM. B. Example of such a ring structure for a source-reconstruction plane distance,  $R$ , of  $840 \mu\text{m}$  and a wavelength of  $307 \text{ nm}$ .

In a phase reconstruction the maximum phase shift that is plotted is  $2\pi$  so that when this value is reached, the phase is set back to zero. This implies that the phase reconstruction will appear as a concentric set of phase rings. The number of rings within the distance,  $w$ , is then given by

$$N = \Phi/2\pi. \quad (3)$$

An example of such a ring structure in a phase reconstruction is shown in Fig. 1B.

The phase varies between 0 (dark) and  $2\pi$  (light) and shows many phase jumps that form concentric rings with the phase changing by  $2\pi$  from ring to ring. This ring structure then provides a natural conversion scale of phase as intensity to phase in terms of radians. A phase reconstruction of a hologram with a sample in place will show this circular structure with the sample phase information superimposed. Reconstruction of a blank or background hologram at the same source–object distance (SOD) as used for imaging of a sample shows an identical ring structure but without any sample information. This background phase pattern can thus be eliminated by simply subtracting the background hologram phase reconstruction from the sample hologram reconstruction. After such a subtraction, the sample phase information will be superimposed on a nearly flat phase background. All phase images were obtained by reconstructing individual holograms and not contrast holograms.

In this study our interest is in measuring the relative phase shifts when transparent objects with refractive index  $n_{\text{obj}}$  are immersed in a fluid of refractive index  $n_f$ . The phase shift depends on the distance that light travels in each medium. For light with wavelength  $\lambda_0$  traveling a distance  $t$ , in the object, the relative phase shift is given by

$$\Delta\psi = (n_{\text{obj}} - n_f)2\pi t/\lambda_0. \quad (4)$$

The optic path difference (OP) is defined as

$$\text{OP} = (n_{\text{obj}} - n_f)t = (\lambda_0 \Delta\psi)/(2\pi). \quad (5)$$

Cuts through a phase reconstruction image of an object thus make it possible to determine the optic path as function of position within the objects. If the extent of an object in the light propagation direction is known, the refractive index difference can be calculated from the measured phase shifts by inverting Eq. (4). Alternatively, knowledge of the refractive indexes allows a determination of the object extent in the light propagation direction (object height). Since the lateral dimensions of an object can be determined from the phase or intensity image directly, the object volume can be determined.

## 2. Experimental Arrangement and Preparation of Samples and Simulated Holograms for PSDIHM Phase Measurements

All PSDIHM measurements were made with a tabletop PSDIHM from Resolution Optics, Inc. (RO) [10]. The component arrangements in that instrument are shown in Fig. 2. A small 25 mw laser ( $\lambda = 405 \text{ nm}$ ) is incorporated in the housing of a standard 100× microscope objective. The laser beam with a beam divergence  $<0.6 \times 0.3 \text{ mrad}$  is focused by the objective lens onto a pinhole that is mounted directly in front of the lens at the focal distance. The 4 mm diameter pinhole foil is mounted on a support ring as shown. To align the  $0.5 \mu\text{m}$  diameter pinhole with the focus point of the objective, the support ring is nudged laterally until optimum light transmission is achieved. At that point, the ring is glued in place. The point source is mounted below a standard optical microscope sample stage that allows  $X$ ,  $Y$ , and  $Z$  movement of the sample over the pinhole. The  $Z$  movement of this stage is used to vary the SOD. The hologram is directly recorded on the sensor chip of a CCD camera that is mounted on a  $Z$  stage so that the source–screen distance (SSD) can be varied. The CCD camera was a Toshiba Teli CSB 4000F ( $2048 \times 2048$ ,  $6.0 \mu\text{m}$  pixels). As is evident from Fig. 2, the equipment part of PSDIHM is extremely simple and point-source DIHM can just as easily be carried out with individual components arranged on an optical bench. In such a setup (most of our previous work on PSDIHM was done that way), the laser illuminates an objective in a standard spacial filter unit and the spherical wave emanating from the pinhole of the filter illuminates the sample to form a hologram on a CCD camera chip a short distance away.

Holograms were reconstructed with RO software Holosuite 2011 which uses the Helmholtz–Kirchhoff transform as discussed above. All reconstructions were done with an effective wavelength as discussed

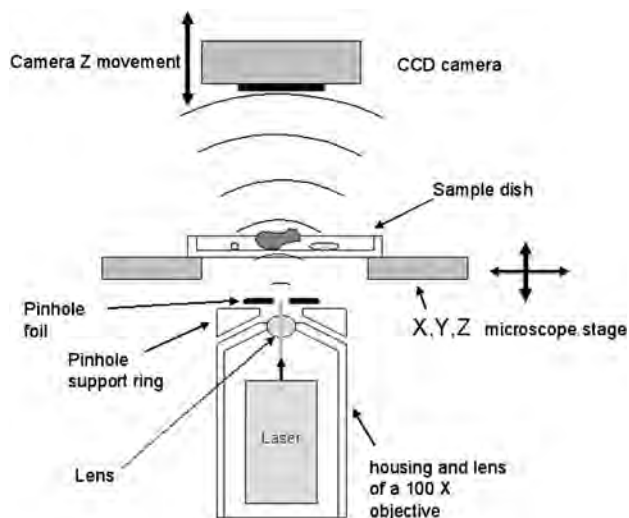


Fig. 2. Schematic of the component arrangement for the point-source digital in-line holographic microscope from Resolution Optics, Inc. that was used for the experiments reported in this work.

by Jericho *et al.* [9]. The fast reconstruction time of 10 ms per image plane (with  $2048 \times 2048$  pixels) allowed easy focusing of objects so that intensity, amplitude, or phase image reconstructions could be obtained rapidly. Phase images were analyzed with RO software by taking single or multiple cross sections of an image. All phase measurements represent the difference in phase shifts between the object and the suspending medium. The optical path through the object was then calculated from Eq. (5).

For biological objects, we chose live organisms such as floating HeLa cells (spheres), floating fibroblast cells (spheres), and fibroblast cells attached to substrates (disklike), as well as *E. coli* bacteria (rodlike) that were colonizing a substrate in early stage biofilm formation.

#### A. Simulated Holograms

Simulated holograms were prepared for transparent objects of standard geometry such as spheres, rods, and plates that were immersed in water. In the simulation (as for all real objects investigated) the objects were placed on a large  $170 \mu\text{m}$  thick cover slip with refractive index  $n = 1.53$ . The refractive indexes of the objects were chosen such that the index jumps from water to object were comparable to those encountered in real samples such as biological cells. Index values and object size along the optic path was also arranged to produce phase shifts that minimized phase wrappings. In the simulations an 800 nm diameter pinhole illuminated by a 408 nm laser served as a light source. SODs, as well as SSDs, were also comparable to typical distances used with our high-resolution PSDIHM microscope setups. A meaningful comparison of PSDIHM intensity and phase reconstructions of simulated holograms with reconstructions of holograms of actual objects should thus be possible.

The simulations are based on the Kirchhoff approximation in which the wavefront above the object is given by  $U(x, y, z+) = t(x, y)U(x, y, z-)$  where  $U(x, y, z-)$  is the wavefront below the object, and  $t(x, y)$  is the object transmission function. Objects that are 3D are sliced into a set of such parallel Kirchhoff planes with an axial spacing less than the wave length and the object thickness. The propagation of the wave field from the object planes to the detector are done with the first Rayleigh Sommerfeld integral [11] or alternatively with the Kirchhoff-Helmholtz transformation Eq. (1).

#### B. Glycerin in Oil

Glycerin drops in type A microscope oil were prepared by adding  $100 \mu\text{l}$  of glycerin to 1 ml of oil. This mixture was then vortexed for 15 min and a small sample of the resulting suspension was placed between two cover slips. This preparation method produced glycerin drops in the 1 to  $10 \mu\text{m}$  diameter size range. The drop size was determined with both PSDIHM as well as with optical phase microscopy on a Leica DM-IRE2 HC inverted microscope.

#### C. Optic Fibers

We investigated the single mode optic fiber F-SV from Newport Corp. This fiber is designed for 633 nm light and has a nominal core diameter of  $\sim 4 \mu\text{m}$  and a cladding diameter of  $125 \mu\text{m}$ . The refractive indexes of cladding and core were 1.4570 and 1.46195, respectively, as supplied by the manufacturer. The optic path through the cladding is thus much larger than that through the core. In order to see core effects, the fiber was suspended in index matching oil. The protective outer coating was removed and the fiber was imaged in a small cell that could be filled with oil of known refractive index. The fiber was introduced to the imaging cell through a small diameter syringe needle. After recording the PSDIHM hologram, this arrangement made it possible to withdrawn the fiber from the cell in order to record the reference hologram with minimum perturbation of the oil in the cell. The oils used were purchased from Cargille Laboratories and had refractive indexes that increased in steps of 0.002.

#### D. *E. coli* Bacteria

DIHM imaging of *E. coli* bacteria was done with a flow cell. Luria Bertani growth medium flowed through the cell at a speed of a few millimeters per second. Under these conditions bacteria tend to colonize the flow cell windows in an attempt to form biofilms. Imaging was performed at the initial stage of biofilm formation where some bacteria were already firmly attached while others still showed lateral movement of several micrometers as determined from hologram sequences.

#### E. HeLa Cells

Live HeLa cells were imaged in a standard plastic Petri dish. The cells were suspended in buffer that had a depth of about 3–4 mm. A hologram generally contained information about both attached and floating cells.

#### F. Fibroblast Cells

Cells were human airways smooth muscle cells, which are very similar to 3T3 cells. A small drop of a cell suspension in Hams S12 growth medium was sandwiched between two cover slips. The edges of the cover slips were sealed with fast drying varnish and both attached and floating cells were imaged. Experiments were done on freshly prepared cells over a period of two hours.

### 3. Results

#### A. Phase Reconstructions from Experimental and Simulated Holograms

The reconstructions of simulated and experimental holograms were first performed in intensity mode to determine the in focus plane of the objects. The corresponding phase reconstructions of the objects were then created. Images were analyzed by taking cuts through the phase images. These cuts showed

the variation of the integrated value of  $\Delta\psi = (\psi_{\text{object}} - \psi_{\text{water}})$  as function of position within the objects where  $\psi$  is the phase shift in radians. In a phase image, the immediate vicinity of objects at times showed phase oscillations (residual phase fringes) that made it difficult to decide on a baseline from which to measure the phase changes. In most cases, except where indicated, the phase shifts were therefore measured relative to regions where the background was flat and at the nominal phase zero level.

## B. Spherical Objects

### 1. Simulation

Figure 3A shows the setup used for the creation of simulated holograms for a transparent 15  $\mu\text{m}$  diameter sphere with refractive index  $n = 1.36$  immersed in water. Figure 3B shows the reconstructed phase image of the sphere. The variation of the phase through a central section of the sphere obtained from this phase image is shown in Fig. 3C. The background on either side of the sphere, except for some weak background fringes visible in Fig. 3B, is essentially flat, and the phase shift, as function of position inside the sphere, follows a smooth and noise free path. The largest phase shift through the sphere from Fig. 3C is 6.92 (rad). From the simulation parameters in Fig. 3C the expected maximum OP is 6.93 (rad). The agreement is thus excellent. The phase variation in Fig. 3C should follow the thickness variation of the sphere in a central plane. The phase should thus depend on the distance from the sphere center,  $X$ , according to  $\Delta\psi_{\text{sphere}} = (4\pi/\lambda_0) * \Delta n * (R^2 - X^2)^{1/2}$ . This expression is also plotted in Fig. 3C (circles) and the fit with the PSDIHM phase reconstruction of the simulated hologram of the sphere is excellent.

### 2. Glycerin Drops in Oil

Figure 4A is a phase image of a number of micrometer-sized drops of glycerin suspended in type A microscope oil. The selected drops were about 4  $\mu\text{m}$  in diameter as determined from PSDIHM intensity images as well as phase images with the Leica microscope. Examples of the variation of the integrated phase through the drops are shown in Fig. 4B for drops 1 and 2. All drops examined showed relatively noise free cross-sections and little phase variation of the background. From the known refractive index difference ( $\Delta n = 0.042$ ) between glycerin and type A microscope oil and with the measured maximum phase shifts for a drop, we can calculate the drop height. The results for the four drops shown in Fig. 4A are presented in Table 1. From the table we see that the drop heights are between 3 and 4  $\mu\text{m}$ . Determination of the drop diameters from the PSDIHM intensity image that is complementary to the phase image of Fig 4A is complicated. The phase cuts seen in Fig. 4B show considerable widening near the base and suggest larger drop diameters than expected from our optical images of the drops obtained with the Leica microscope. This broadening is also ob-

served, but to a lesser extent, for intensity cuts. To compare the trend between drop size measurements from phase changes with drop sizes obtained from intensity images, we linearly extrapolated the sides of the intensity peaks back to the baseline and took the distance between the intersection points to represent the drop diameter. These values are also given in Table 1. As Table 1 shows, except for drop 1, the agreement between drop height calculated from the maximum phase shift and the diameter obtained from intensity reconstructions is within  $\sim 10\%$ . The apparent disagreement for drop 1 could be related to stronger substrate adhesion for drop 1.

### 3. Fibroblast Cells

Fibroblast cell cultures showed floating and attached cells. Floating cells appeared to have a spherical shape, while attached cells flattened and spread out over the substrate surface. Figure 5A is a phase image showing both a spherical floating cell and an attached cell at (b) that is in the process of extending its filopodia. The phase shift through the floating fibroblast cell exceeds  $2\pi$  so that phase wrapping takes place. The unwrapped phase cut through the floating cell is shown in Fig. 5B, while Fig. 5C illustrates the phase shifts after phase unwrapping. Figure 5D shows a phase cut through the center of the attached cell at (b). This phase cut does not show the characteristic phase wrapping signature but instead shows a phase jump as indicated by the arrow.

The diameter of the floating cell from Fig. 5C is  $17 \pm 1 \mu\text{m}$ . If we assume a spherical shape for this cell, then we can calculate the refractive index difference between the external fluid and the cell interior. The refractive index of standard growth medium for mammalian cells, because of salts and nutritional additives, is somewhat larger than that of water and is about 1.337 [12]. The maximum phase shift from Fig. 5C is 7.11 (rad), which then gives a refractive index difference of  $\Delta n = 0.027$  or an integrated refractive index for the cell interior of  $n_{\text{fibroblast}} = 1.364 \pm 0.001$ . This value is within the limits quoted by Lanni *et al.* for 3T3 fibroblast cells (1.358 – 1.374) [13] but is larger than that measured by Lee *et al.* for 3T3 cells ( $\sim 1.3506$ ) [12]. If we assume that the 29  $\mu\text{m}$  diameter flat cell at (b) in Fig. 5A has the same volume as the floating cell at (a), then the thickness of the cell at (b) must be around 3.9  $\mu\text{m}$  so that the cell experienced considerable flattening. As shown in Fig. 5C, this cell flattening resulted in an unexpected form of the phase cut. The phase shows a strong decrease as the cell is approached from outside and then shows a large phase jump inside the cell. This point will be discussed in Section 3.D in connection with phase imaging of disks.

### 4. HeLa Cells

Cultures of HeLa cells contained both mobile as well as nonmobile cells. Floating HeLa cells are spherical in shape and were drifting rapidly in the suspension. Many cells were stationary and were attached to the

substrate while some drifted slowly in close proximity to the substrate. Only the slow moving, as well as stationary cells, were analyzed. A phase image of a nonmobile HeLa cell is shown in Fig. 6A. A cut through the center of this phase image is shown in

Fig. 6B and is represented as the phase variation as function of position. As for floating fibroblast cells, the phase change was larger than  $2\pi$  and the phase had to be unwrapped. A phase image of two slowly moving cells is shown in Fig. 6C while the

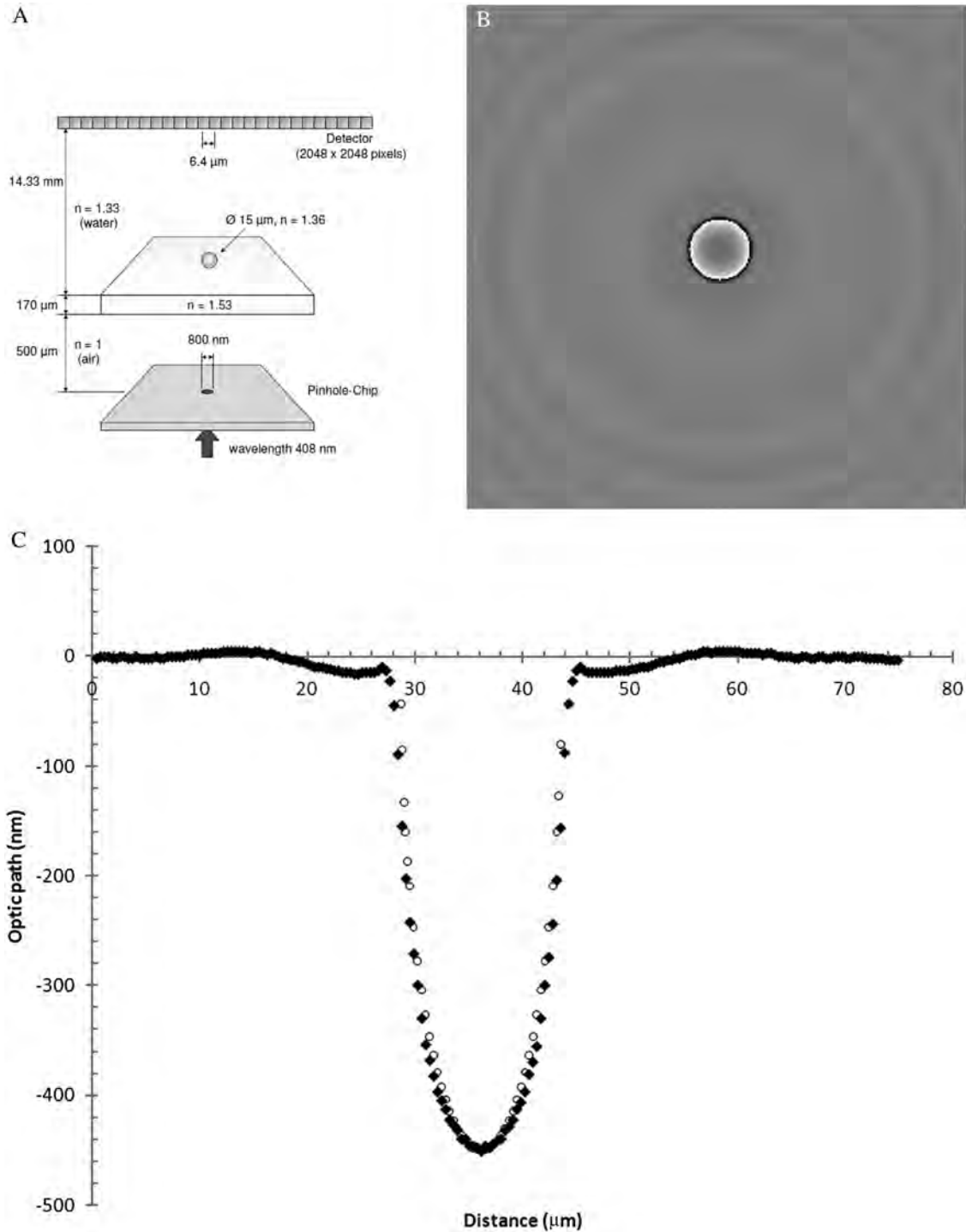


Fig. 3. Analysis of a simulated hologram for a sphere. A. Setup for the calculation of a hologram of a 15 μm diameter sphere placed on a 170 μm thick coverslip and immersed in water. The point source is an 800 nm diameter hole illuminated by 408 nm wavelength coherent radiation. The detector is a 2048 × 2048 array of 6.4 μm square pixels. B. Phase reconstruction of the simulated hologram. Image is reconstructed at an effective wavelength of 307 nm. C. Phase variation along a 75 μm long path through the center of the sphere in C (diamonds). Calculated phase variation from the refractive index difference and sphere size as given in the setup diagram A (open circles). The agreement is excellent.

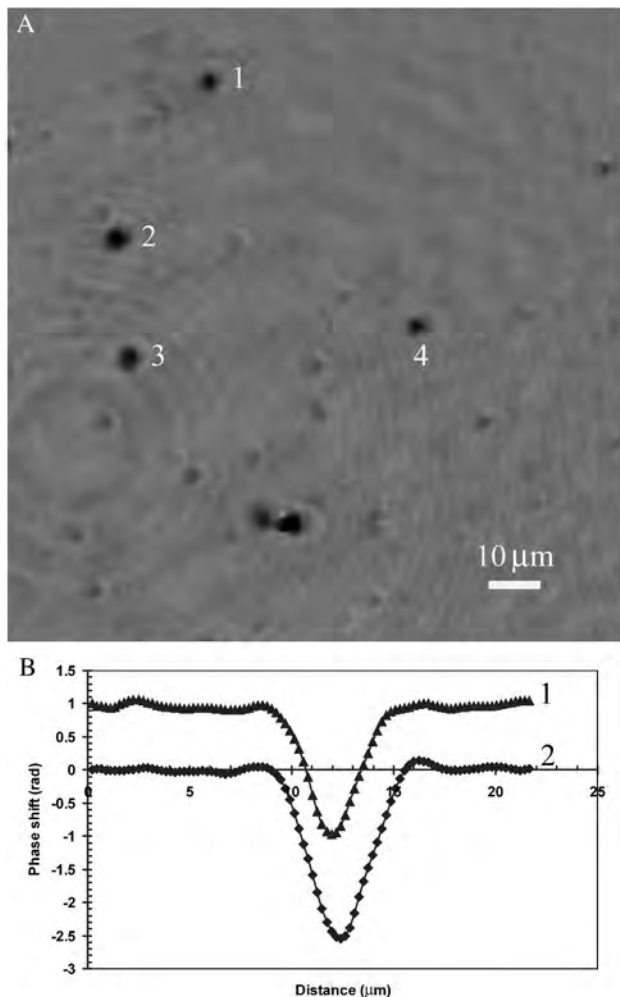


Fig. 4. A. Phase image of four glycerin drops in type A microscope oil. Bar = 10  $\mu\text{m}$ . Imaging conditions: SOD = 745  $\mu\text{m}$ , SSD = 20 mm,  $\lambda = 405$  nm. B. Phase cuts through drops 1 and 2 in A with trace 1 shifted upward by one radian for clarity.

corresponding unwrapped optic path variation of the cell on the left is shown in Fig. 6D. It is interesting to note that the mobile cell has a phase shift almost 40% higher than the nonmobile cell. The refractive index of HeLa cells was measured previously by Lue *et al.* [14] who obtained  $n = 1.385$ . With this value for the refractive index of the HeLa cell's cytoplasm, the refractive index difference,  $\Delta n$ , has the value 0.047. The phase maximum for the attached cell in Fig. 6B is 7.6 (rad) which then gives, with

Eq. (5), a cell height of 10.4  $\mu\text{m}$ . This is considerably smaller than the lateral size of the cell and suggests considerable cell flattening when cells are attached to a substrate. The phase maximum for the slowly moving cell in Fig. 6C is at 11.25 rad and indicates a cell height of 15.4  $\mu\text{m}$ . Although this value is larger, the slowly moving cells may already sense the proximity of the substrate surface and weak cell attachment may already have flattened such cells.

### C. Rods

#### 1. Simulation

Figure 7A shows the arrangement of point source, sample, and CCD detector for the simulated hologram of a 5  $\mu\text{m}$  diameter transparent fiber. Laser wavelength, distances, and CCD pixel size are very similar to the arrangement that was used for actual PSDIHM imaging of a fiber (see Fig. 8). The refractive index difference between the fiber and the surrounding water was chosen to be 0.05 in order to avoid phase wrapping. Figure 7B shows a hologram of the fiber and Fig. 7C a reconstructed intensity image. Figure 7D gives the corresponding phase image, while Fig. 7E shows the variation of the integrated phase along a cross-section of the fiber for the phase image of Fig. 7D. From Fig. 7E the maximum phase shift relative to background is 4.0 rad. The maximum phase shift expected from the parameters indicated in Fig. 7A is 3.85 rad, which is about 3.8% lower than the value obtained from the PSDIHM phase reconstruction of the simulated hologram.

#### 2. Single-Mode Optic Fiber

Figure 8A shows the phase image of a 125  $\mu\text{m}$  diameter fiber ( $n_{\text{cladding}} = 1.45702$  and  $n_{\text{core}} = 1.46195$ ) immersed in matching oil with  $n_{\text{oil}} = 1.4560$ . At this level of index matching, (-0.001), the cladding boundaries are still visible as broad ridges and the core region is easily identified as a thin line at the center of the fiber. A long cut taken perpendicular to the whole fiber is shown in Fig. 8B and clearly shows phase changes at the cladding surface as well as sharp phase changes as the fiber core is traversed. As is evident from Fig. 8B, the cladding part of the fiber did not show the expected signature for a rod but instead only gave significant phase variation near the rod outer periphery at  $L$  and  $R$ . The phase then decayed in a roughly parabolic fashion towards the core region so that the core signature, as shown

Table 1. Comparison of Glycerin Drop Size as Determined from Phase Shifts and from Intensity Reconstructions<sup>a</sup>

Glycerin Drop from Fig. 4A	Maximum Phase Shift (rad)	Drop Height from Phase Shift ( $\mu\text{m}$ )	Drop Diameter from Intensity Image ( $\mu\text{m}$ )
1	$2.0 \pm 0.2$	$3.1 \pm 0.3$	4.0
2	$2.52 \pm 0.2$	$3.9 \pm 0.3$	4.0
3	$2.50 \pm 0.2$	$3.8 \pm 0.3$	4.2
4	$2.26 \pm 0.2$	$3.5 \pm 0.3$	3.3

$\Delta n = (n_{\text{glyc}} - n_{\text{oil}}) = 0.042$

<sup>a</sup>The maximum phase shift is the average calculated from several phase cuts through each drop. The errors represent the sample standard error. Errors for drop height represent the error contributions from these phase errors.

in Fig. 8B, appeared to be superimposed on this parabolic background. An average of ten cuts through the core region is presented in Fig. 8C. The phase signature of the rodlike core region is easily mapped even

though the refractive index difference relative to the cladding is only 0.00493. Figure 8C suggests a core diameter that is consistent with the value of  $4\ \mu\text{m}$  supplied by the manufacturer although the core base

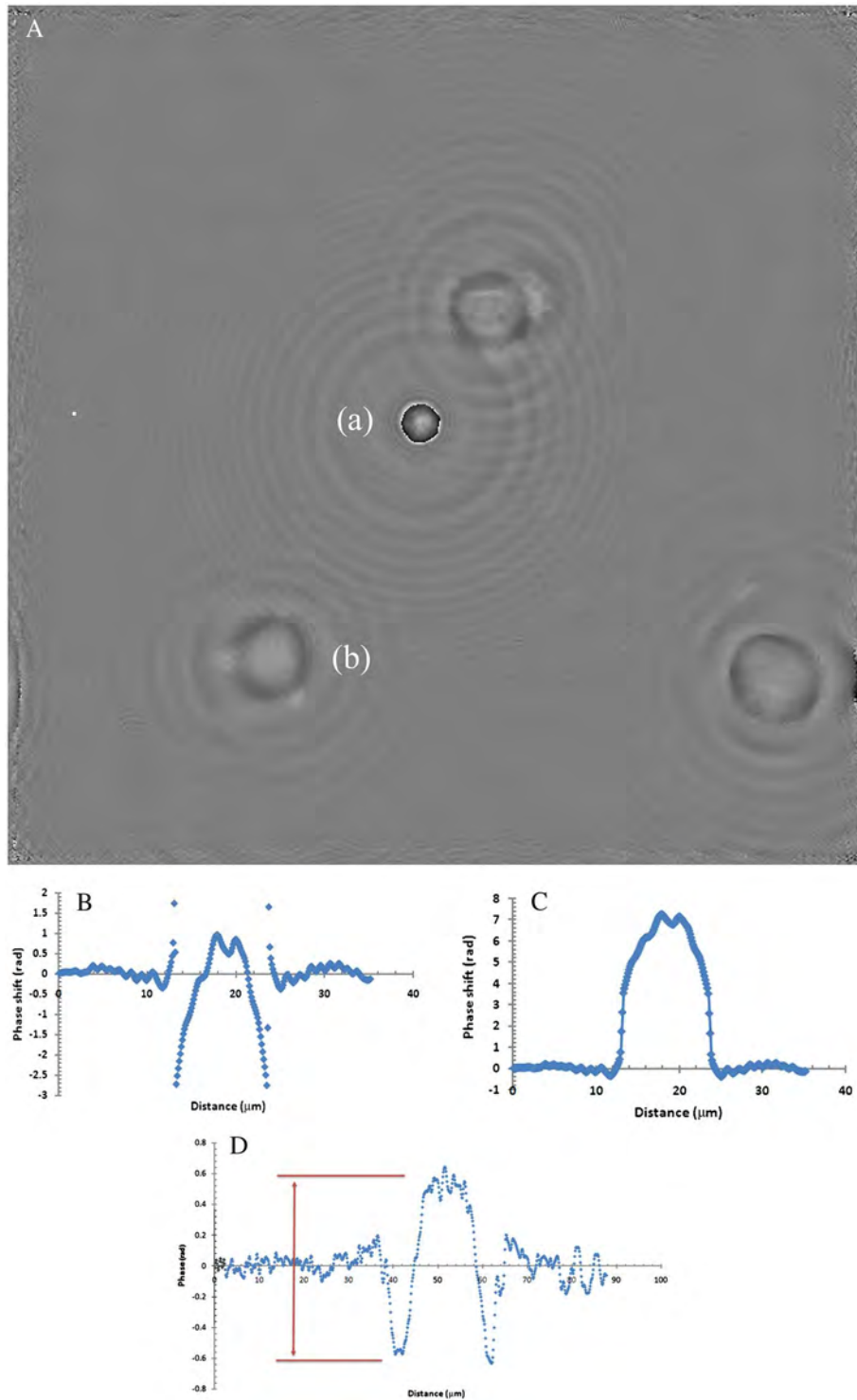


Fig. 5. (Color online) A. Phase image of four fibroblast cells in growth medium. The cell at a is a floating cell and such cells are known to be spherical in shape. Cell at (b) has a larger diameter and is in the process of attaching to the substrate surface. Imaging parameters: SSD = 20 mm, SOD =  $560\ \mu\text{m}$ ,  $\lambda = 405\ \text{nm}$ . B. Phase cut through the center of cell at (a). The cut shows the characteristic signature of a  $2\pi$  phase wrap. C. Unwrapped phase image of cell (a). D. Phase cut through center of cell at (b). The phase initially decreases as the cell edge is approached and then shows a phase jump indicated by the arrow. The phase changes for this cell are much smaller than the phase changes for the cell at (a) and suggests a flattened cell.

appears somewhat wider in Fig. 8C. The phase near the core region appears to be at background level and the zero for the phase plot in Fig. 8C was obtained by taking a simple regression average of a 60  $\mu\text{m}$  wide region near the core base with the core itself not included. With this base the maximum phase shift for the core was  $\Delta\Phi = 0.303$  (rad). For a core diameter of 4  $\mu\text{m}$  and a core/cladding refractive index difference of 0.00493, the expected maximum phase shift is  $\Delta\Phi = 0.306$  (rad).

### 3. *E. coli* Bacteria

A phase image of *E. coli* bacteria taken from an image sequence is shown in Fig. 9A. The bacteria with a diameter of about  $\sim 1$   $\mu\text{m}$  are in growth medium with refractive index  $n \sim 1.337$  and are attached to a glass substrate. Several bacteria changed their positions in different frames of the hologram sequence, but exposure times were sufficiently short so that sharp phase images could be obtained. Three phase cuts

perpendicular to the marked (arrow) bacterium were taken and averaged. The result is shown in Fig. 9B. As is evident from Fig. 9B, the observed integrated phase for the bacterium has the variation expected for a rod-type structure and is thus very similar to the phase cut shown in Fig. 7E. The maximum phase shift for the bacterium was  $\Delta\Phi = 0.847$  (rad). From Fig. 9B we estimate the diameter of the bacterium as 0.85  $\mu\text{m}$ . The phase shift then gives a refractive index difference for the *E. coli* cytoplasm of  $\Delta n = 0.0642$ . With a refractive index for the growth medium of  $n_{\text{med}} = 1.337$ , we then obtain for the *E. coli* cytoplasmic refractive index a value of  $n = 1.401$ . Refractive indexes of microorganisms are seldom measured on single individuals. Instead, the optical measurements are generally performed by light scattering experiments on suspensions of organisms and data analysis is performed with Mie scattering theory, which involves the optical density of the suspension, the radius of the particles, and complex Mie

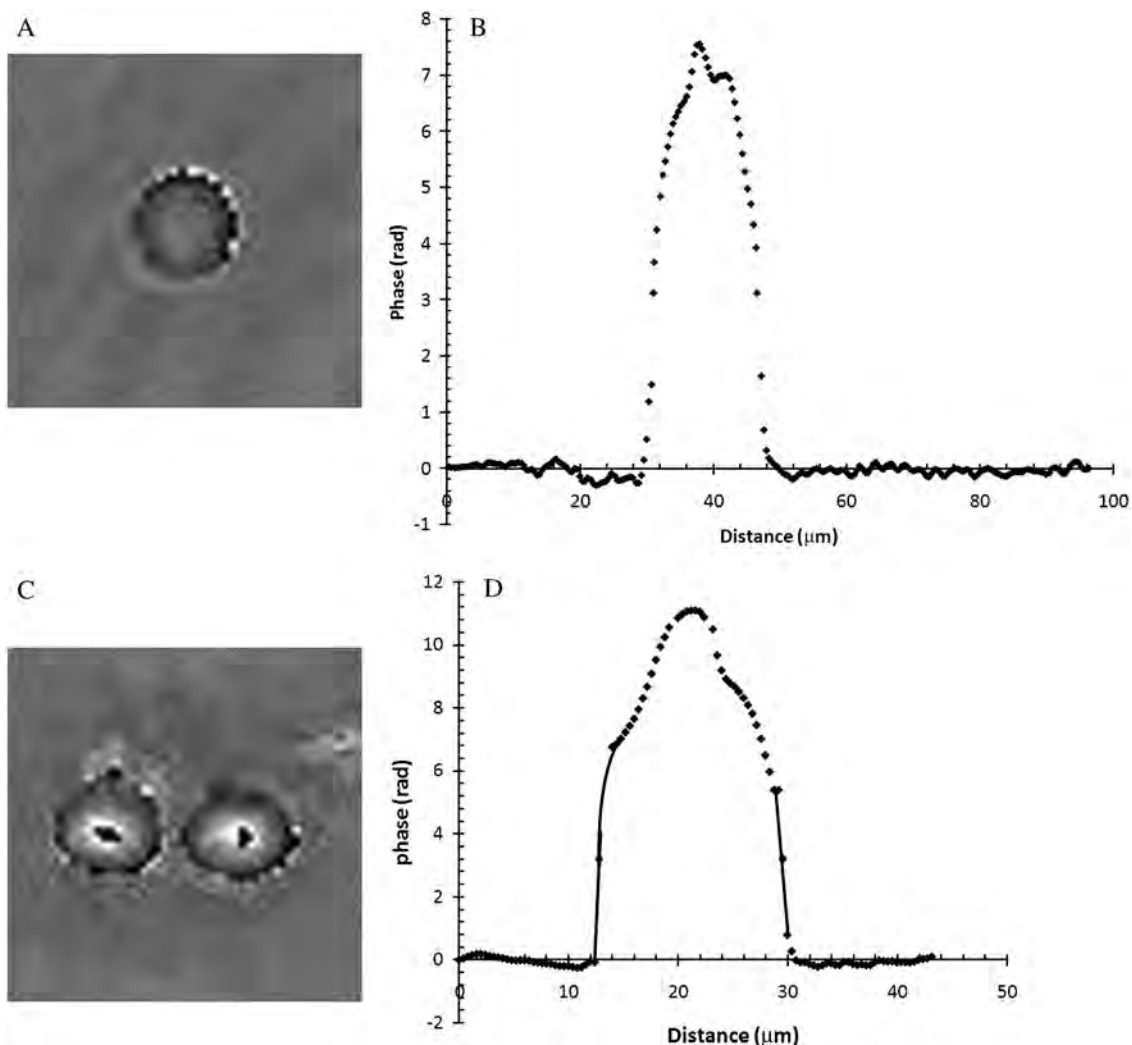


Fig. 6. A. Phase image of an attached HeLa cell. Imaging parameters: SSD = 19.4 mm, SOD = 1287  $\mu\text{m}$ ,  $\lambda_{\text{eff}} = 388$ . B. Unwrapped phase cut through center of cell at A. C. Phase image of two HeLa cells in close proximity of the substrate surface. Imaging parameters: SSD = 19.4 mm, SOD = 1287  $\mu\text{m}$ ,  $\lambda_{\text{eff}} = 388$  nm. D. Unwrapped phase cut through the cell on the left. The phase shifts for the mobile cells in C. were larger than the phase shifts for the attached cell in A.

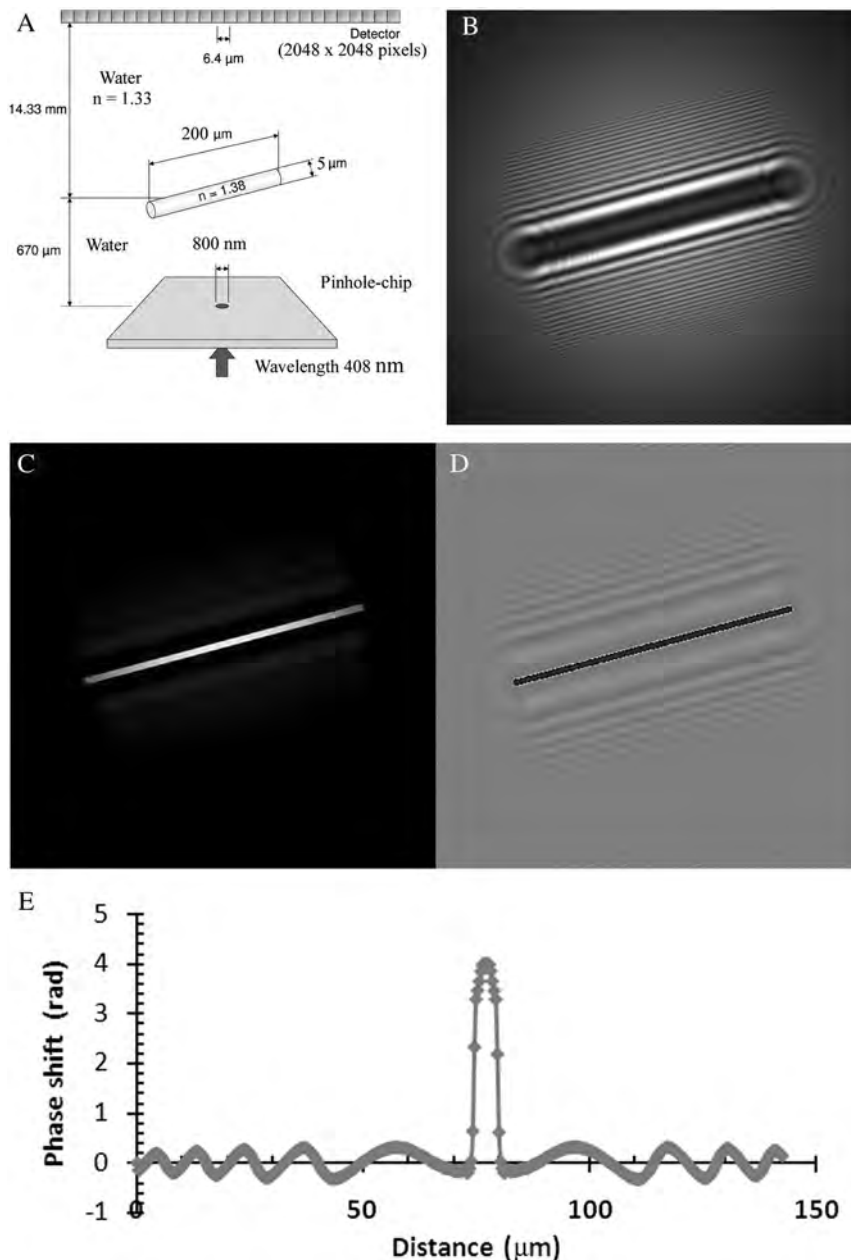


Fig. 7. Analysis of simulated hologram of a transparent rod immersed in water. A. Setup used to generate the hologram. B. Calculated hologram for a  $5\ \mu\text{m}$  diameter rod with  $n = 1.38$ . C. Intensity reconstruction of the rod. D. Phase reconstruction of the rod. E. Phase cut perpendicular to the rod shown in D. The large phase shift from the rod is superimposed on a pattern of phase oscillations on either side of the rod so that the flat background phase is obtained only a few hundred micrometers from the rod. This phase signature is characteristic for thin rods.

scattering functions. Using this approach Kononenko *et al.* [15] obtained a refractive index (at  $\lambda = 400\ \text{nm}$ ) for *E. coli* bacteria of  $n = 1.465$ . This is considerably larger than our measurements. Kononenko also reported a 40% change in the bacterial refractive index between live and dead cells. Phase cuts through different bacteria in Fig. 9A showed considerable variation of the maximum phase shift values. These variations may have been influenced by the size of background fringes in the vicinity of a bacterium. For the image in Fig. 9A, cross sections taken over five bacteria, for example, give a  $\Delta\Phi = 0.908$  with a standard deviation of  $\pm 0.21$  which leads to a pos-

sible bacterial refractive index range of  $n = 1.385$  to  $n = 1.420$ . In terms of phase shifts, live and dead bacteria should have a phase shift difference of almost a factor of two [15]. We think with reconstructions that show background areas relatively free of extra fringes, PSDIHM phase measurements should be able to differentiate between live and dead bacteria.

#### D. Disks

##### 1. Simulation

Many object shapes encountered in microscopy can be approximated by disks. Figure 10A shows the arrangement used for the hologram simulation of

two  $20\ \mu\text{m}$  diameter and  $5\ \mu\text{m}$  thick disks that sit on top of a coverslip support immersed in water. The phase image of the disks is shown in Fig. 10B, while Fig. 10C shows the optic path variation along a cut through the center of one of the disks. This phase

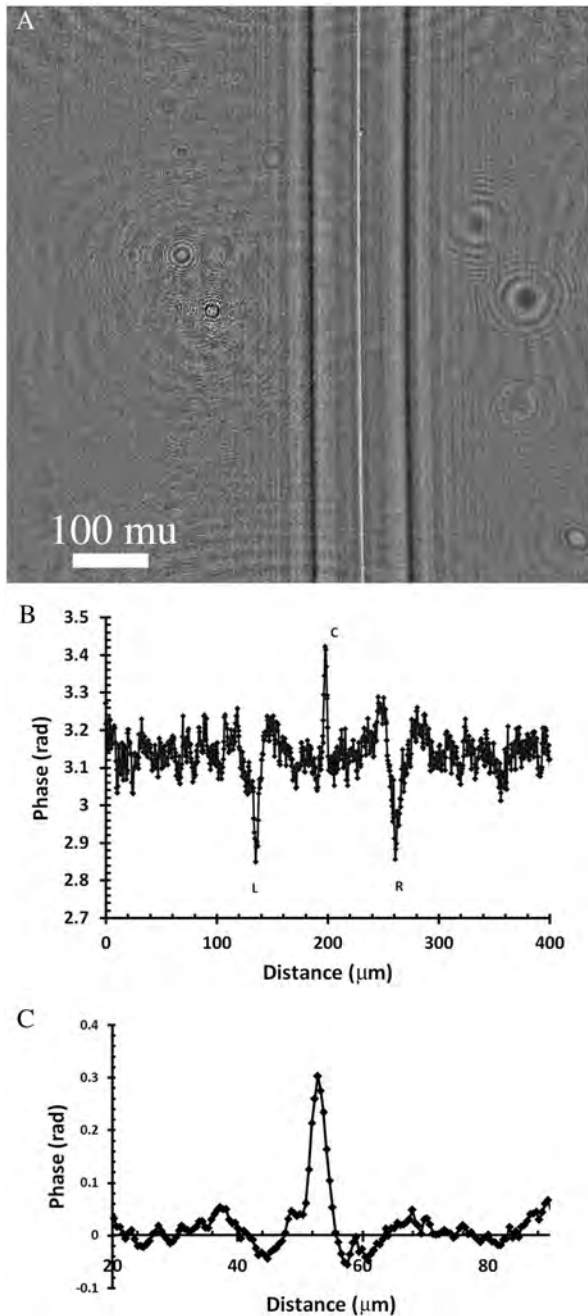


Fig. 8. A. Phase reconstruction of a single mode (633 nm) optic fiber. Nominal cladding and core diameters were  $125$  and  $4\ \mu\text{m}$ , respectively. The fiber was immersed in index matching oil to reduce phase shifts from the cladding. The refractive index jump from cladding to core of  $\Delta n = 0.00493$  is clearly visible as the thin white line running down the middle of the fiber. B. Phase cut perpendicular to the fiber. The edges of the cladding show up as phase dips at  $L$  and  $R$  while the core region at  $C$  has the characteristic phase signature of a thin rod. C. An average of ten phase cuts perpendicular to the fiber core taken at equal intervals along the fiber.

signature does not have the characteristic signature of a phase wrap but shows, after an initial decrease, a large phase jump of  $3.19$  rad as we go from disk edge to center. Standard Fresnel diffraction theory for the edge of a transparent half-plane predicts a phase jump that depends on the refractive index change at the edge [16]. Although the phase jump in Fig. 10C seems more complex than suggested by [16], it is interesting to note that this phase jump, together with a refractive index difference between water and disk of  $0.05$ , would imply a disk thickness of  $4.14\ \mu\text{m}$  which is not too far from the actual  $5\ \mu\text{m}$  thickness of the disks. A preliminary study of phase changes near edges of phase reconstructed transparent plates suggests that, for plates that are less than a few micrometers thick, the phase jump signature of Fig. 10C gives reasonable thicknesses for such plates. Investigations to determine the theoretical underpinnings of these observations are continuing.

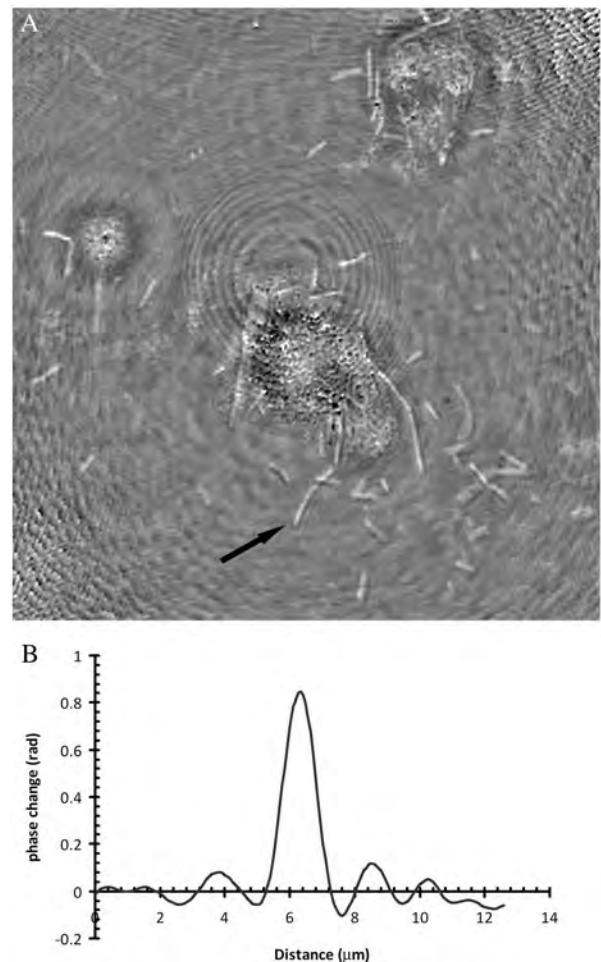


Fig. 9. A. Phase reconstruction of a hologram of *E. coli* bacteria in the initial phases of biofilm formation. Imaging conditions: SSD =  $15$  mm, SOD =  $285\ \mu\text{m}$ ,  $\lambda = 397$  nm. B. Average of three phase cuts taken perpendicular to the bacterium marked by the arrow in A. The phase signature is characteristic for a thin rod and shows background oscillations on either side of the phase shift peak from the bacterium.

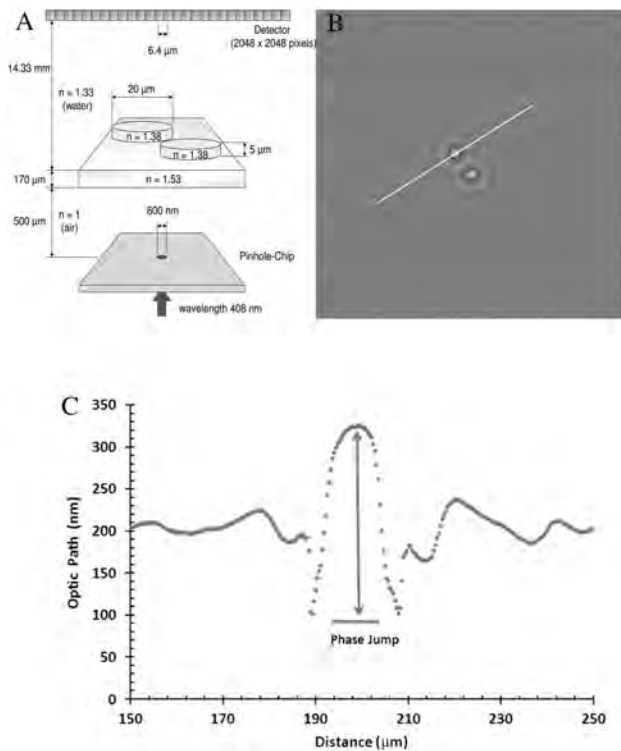


Fig. 10. A. Setup for hologram simulation of two  $20\ \mu\text{m}$  diameter disks. B. Phase reconstruction of the disks. C. Phase cut through center of one disk along line indicated in B. Besides some background oscillations, the main signature is the phase jump (arrow). This jump signature is very similar to the phase variation through the flattened cell (disklike) of Fig. 5D. This phase jump at a refractive index discontinuity, such as the edge of a plate, may allow estimates of the plate thickness.

## 2. Attached Fibroblast Cells

After attaching to a surface, fibroblast cells tend to flatten and spread out over the substrate surface. The cell at (b) in Fig. 5A, as well as the other two unlabeled cells in the image, are cells that have attached and that started to flatten so that their diameters are larger than the floating cell at (a). The phase cut through the center of the cell at (b) is shown in Fig. 5D. This phase cut has a striking resemblance with that shown in Fig. 10C for the simulated holograms for disks. This is perhaps not surprising, since on flattening, a sphere will transform into a disk. The phase jump indicated in Fig. 5D might then allow estimates of the thickness of the flattened cell. The phase jump has a magnitude of  $1.35\ \text{rad}$ . If  $\Delta n = 0.024$  then with  $n_{\text{medium}} = 1.337$  the thickness of the flattened cell is  $\sim 3.5\ \mu\text{m}$ . This is not unreasonable for a cell that just started the attachment process. That this value for the cell thickness is reasonable can also be seen when it is assumed that the cell volume remains approximately constant on cell attachment. As discussed in connection with Fig. 5D above, from the measured diameters of the cells, and setting the volume of the floating cell at a equal to the volume of the flattened cell at (b), we estimate a thickness of  $\sim 3.9\ \mu\text{m}$  for the flattened cell.

## 4. Discussion

We have examined a variety of samples including spheres, rods, and disks. Our objects had phase shifts of less than  $4\pi$ , and phase shifts agreed with those expected from their refractive index differences (objects immersed in water or core versus cladding in single mode fibers) and their sizes to better than 10%, and depending on the hologram quality, at times better than 4%. For the simulated holograms, the agreement between the input and the measured optic paths was within 2% for spheres and 2% to 4% for thin rods. This suggests that twin image effects on phase images are not as serious as previously suggested [7]. The reason for this is the long distance between twin and real image for PSDIHM with light waves with the typical SOD used for high resolution imaging [1,6].

Phase cuts for larger diameter rods (real or simulated) did not show the optic path variation expected from the rod geometry. In disk shaped objects in water, the simulations suggest that the refractive index difference appears to be best described by a phase jump that is observed in both real and simulated disks at the disk boundary. In general, reconstructions of spheres and micrometer-sized rods gave the best results and phase shifts in these objects seem to be directly proportional to local sample thickness so that if  $\Delta n$  is known, phase measurements can determine the local sample thickness. For large refractive index gradients, such as at the edge of a disk or plate, phase reconstructions show phase jumps that give reasonable estimates of the sample thickness. Further theoretical and experimental work, however, is needed to determine under what conditions accurate optic path values can be deduced from the phase jump. In objects with lateral dimensions  $>100\ \mu\text{m}$ , such as large diameter fibers or plates, phase shifts at the sample edges decay away at distances of about  $20\ \mu\text{m}$  from the sample edges. As in standard optical phase microscopy, a transparent plate is only visible through contrast at the plate edges while the plate interior remains essentially at background. The same effect is observed in Fig. 8B for the cladding of the optical fiber and also for the simulation of a  $125\ \mu\text{m}$  diameter glass fiber (data not shown). In PSDIHM, object phase information is encoded through phase changes at the object edges, and for small objects (all edges) quantitative information to 10% and better can be extracted as the phase reconstructions of the simulated holograms have shown. However, even for small objects, phase information will be difficult to extract if phase shifts are multiples of  $2\pi$  and if the object magnification is insufficient so that the object in the phase image is defined by too few pixels. Our present PSDIHM software has 8 bit resolution. Since phase gradients during phase jumps and phase wrappings can be large, this 8 bit resolution can introduce considerable phase change uncertainties. This is not a serious problem for phase wrapping events since phase wrapping has a distinct signature

but it will have a significant effect on the size of phase jumps and thus on sample thicknesses calculated from the jumps.

## 5. Summary

We have shown with simulated holograms and with detailed measurements on a number of different micrometer-sized samples (suspended drops, optical fibers, as well as organisms of biological interest such as *E. coli* bacteria, HeLa cells and fibroblast cells) that point-source DIHM is ideally suited for quantitative phase measurements to determine optical path lengths and to extract changes in refractive index within an accuracy of 0.001 on the submicrometer length scale. Using a detector with more than 8 bit resolution allows this accuracy to be pushed even further. Another promising extension of this approach is to look at time dependent changes, e.g., in situations where bacteria die.

This work was funded by National Science and Engineering Research Council of Canada (NSERC) and the Office of Naval Research, Washington, DC. Instrument and software support by Resolution Optics, Inc. was of great value. We thank P. Klages for many helpful discussions.

## References

1. W. Xu, M. H. Jericho, I. A. Meinertzhagen, and H. J. Kreuzer, "Digital in-line holography for biological applications," *Proc. Natl. Acad. Sci. USA* **98**, 11301–11305 (2001).
2. J. Garcia-Sucerquia, W. Xu, S. K. Jericho, M. H. Jericho, P. Klages, and H. J. Kreuzer, "Digital in-line holographic microscopy," *Appl. Opt.* **45**, 836–850 (2006).

3. H. J. Kreuzer, M. H. Jericho, I. A. Meinertzhagen, and W. B. Xu, "Digital in-line holography with photons and electrons," *J. Phys. Condens. Matter* **13**, 10729–10741 (2001).
4. M. Kanka, R. Riesenberger, and H. J. Kreuzer, "Reconstruction of high-resolution holographic microscopic images," *Opt. Lett.* **34**, 1162–1164 (2009).
5. H. J. Kreuzer, K. Nakamura, A. Wierzbicki, H.-W. Fink, and H. Schmid, "Theory of the point source electron microscope," *Ultramicroscopy* **45**, 381–403 (1992).
6. M. H. Jericho and H. J. Kreuzer, "Point source digital in-line holographic microscopy," in *Coherent Light Microscopy*, Vol. **46** of Springer Series in Surface Sciences, P. Ferraro, A. Wax, and Z. Zalevsky, eds. (Springer-Verlag, 2011), pp. 3–30.
7. W. Qu, O. C. Chee, Y. Yu, and A. Asundi, "Recording and reconstruction of digital Gabor holograms," *Optik* **121**, 2179–2184 (2010).
8. D. Gabor, "Microscopy by reconstructed wave fronts," *Proc. R. Soc. A* **197**, 454–487 (1949).
9. S. K. Jericho, J. Garcia-Sucerquia, W. Xu, M. H. Jericho, and H. J. Kreuzer, "Submersible digital in-line holographic microscope," *Rev. Sci. Instrum.* **77**, 043706 (2006).
10. [www.resolutionoptics.com](http://www.resolutionoptics.com).
11. A. Wuttig, M. Kanka, H. J. Kreuzer, and R. Ranier, "Packed domain Rayleigh–Sommerfeld wavefield propagation for large targets," *Opt. Express* **18**, 27036–27047 (2010).
12. J. Y. Lee, C. W. Lee, E. H. Lin, and P. K. Wei, "Single live cell refractometer using nanoparticle coated fiber tip," *Appl. Phys. Lett.* **93**, 173110 (2008).
13. F. Lanni, A. S. Waggoner, and D. L. Taylor, "Structural organization of interphase 3T3 fibroblasts studied by total internal reflection fluorescence microscopy," *J. Cell Biol.* **100**, 1091–1102 (1985).
14. N. Lue, G. Popescu, T. Ikeda, R. R. Dasari, K. Badizadegan, and M. S. Feld, "Live cell refractometry using microfluidic devices," *Opt. Lett.* **31**, 2759–2761 (2006).
15. A. P. Kononenko, K. I. Kononenko, and D. M. Mikhov, "Dependence of refractive index on physiological state of microbial population," *Zh. Prikl. Spektrosk.* **11**, 114–117 (1969), translation.
16. S. P. Anokhov, "Plane wave diffraction by a perfectly transparent half-plane," *J. Opt. Soc. Am.* **24**, 2493–2498 (2007).